JOURNAL OF THE AMERICAN CHEMICAL SOCIETY

Article

pubs.acs.org/JACS

Molecular Synthesis of High-Performance Near-IR Photodetectors with Independently Tunable Structural and Optical Properties Based on Si−Ge−Sn

Chi Xu,[‡] Richard T. Beeler,[†] Gordon J. Grzybowski,[†] Andrew V.G. Chizmeshya,[†] David J. Smith,[‡] José Menéndez,[‡] and John Kouvetakis*,[†]

[†]Department of Chemistry and Biochemistry, Arizona State University, Tempe, Arizona 85287-1604, United States

[‡]Department of Physics, Arizona State University, Tempe, Arizona 85287-1504, United States

ABSTRACT: This Article describes the development of an optimized chemistry-based synthesis method, supported by a purpose-built reactor technology, to produce the next generation of $Ge_{1-x-y}Si_xSn_y$ materials on conventional Si(100) and Ge(100) platforms at gas-source molecular epitaxy conditions. Technologically relevant alloy compositions (1−5% Sn, 4−20% Si) are grown at ultralow temperatures (330−290 °C) using highly reactive tetragermane (Ge_4H_{10}), tetrasilane (Si_4H_{10}), and stannane (SnD_4) hydride precursors, allowing the simultaneous increase of Si and Sn content (at a fixed Si/Sn ratio near 4) for the purpose of tuning the bandgap while maintaining lattice-matching to Ge. First principles thermochemistry studies were used to explain stability and reactivity differences between the Si/Ge hydride sources in terms of a complex interplay among the isomeric species, and provide guidance for optimizing process conditions. Collectively, this approach leads to unprecedented control over the substitutional incorporation of Sn into Si−Ge and yields materials with superior quality suitable for transitioning to the device arena. We demonstrate that both intrinsic and doped $Ge_{1-x-y}Si_xSn_y$ layers can now be routinely produced with defect-free microstructure and viable thickness, allowing the fabrication of high-performance photodetectors on Ge(100). Highlights of these new devices include precisely adjustable absorption edges between 0.87 and 1.03 eV, low ideality factors close to unity, and state-of-the-art dark current densities for Ge-based materials. Our unequivocal realization of the "molecules to device" concept implies that GeSiSn alloys represent technologically viable semiconductors that now merit inclusion in the class of ubiquitous Si, Ge, and SiGe group IV systems.

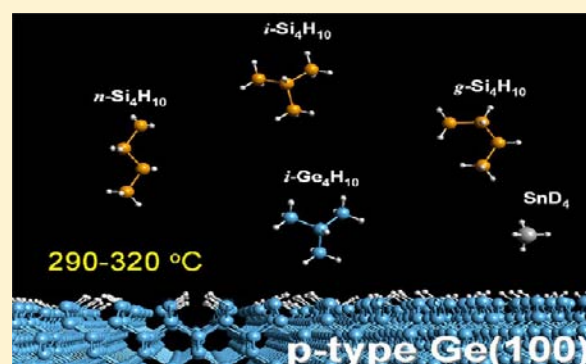

I. INTRODUCTION

For the past 50 years, simple molecular compounds such as silane (SiH_4) and germane (GeH_4) have been the chemical vapor deposition (CVD) precursors of choice in the development of silicon and silicon−germanium technologies, which have dominated the field of electronics. More recently, the need for lower deposition temperatures and more complex group IV materials, such as those incorporating Sn, has stimulated research into higher-order silanes and germanes, most notably digermane (Ge_2H_6), and trisilane (Si_3H_8), as well as Sn compounds such as SnD_4 and $SnCl_4$, which are now commercially available.[1−3] One of the most intriguing byproducts of recent work in this area is the synthesis of crystalline $Ge_{1-x-y}Si_xSn_y$ alloys, which represent the first viable ternary semiconductor system among group IV elements with independently tunable lattice parameter and electronic structure.[4−6] This flexibility confers the material a great potential for multijunction solar cells in which the multiple band gaps must be independently tuned to optimize efficiency, while the lattice parameters must be kept the same across the structure to minimize formation of deleterious defects.[7−9]

The original synthesis of $Ge_{1-x-y}Si_xSn_y$ was conducted via reactions of SiH_3GeH_3 with SnD_4 using ultrahigh vacuum CVD to produce the first generation of samples that allowed thorough initial characterization of the intrinsic properties of the new system to be performed.[10] This approach exploits the high reactivity of SiH_3GeH_3, which is also more compatible with the low temperatures required for growth of single-phase monocrystalline structures with high Sn contents (note that the degree of Sn incorporation and the growth temperature are typically inversely related).[10] The routine use of SiH_3GeH_3 in this process was, however, found to be problematic from a device development perspective because the fixed Si/Ge ratio in the precursor limited stoichiometry control needed to precisely tune alloy compositions with respect to strain. In addition, this compound is not yet commercially available in sufficient quantities and purity to ensure routine large-scale fabrication of thick layers with suitable microstructure and their deployment on large-area platforms as required for high-

Received: October 6, 2012
Published: December 14, 2012

ACS Publications © 2012 American Chemical Society

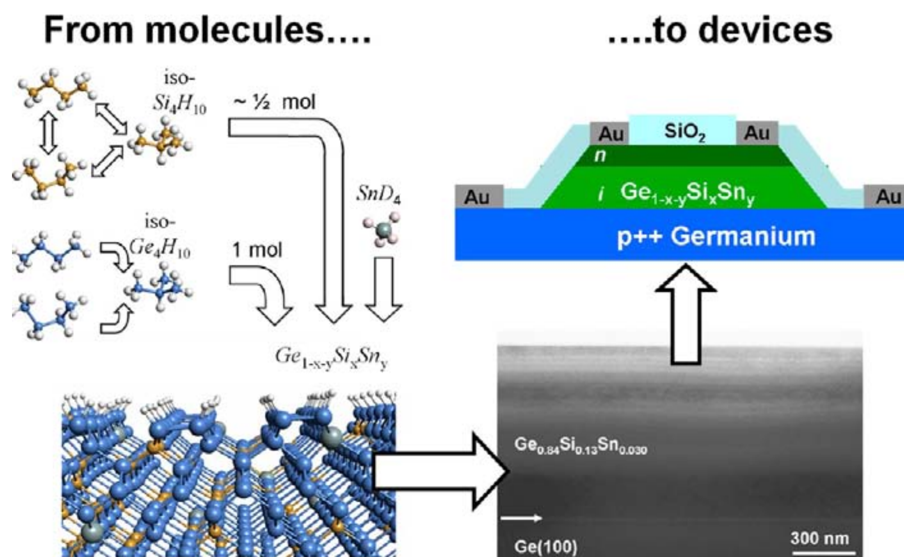

Figure 1. Schematic illustration of the "molecules, to materials, to functional devices" paradigm emphasized in this Article. The reactive Si_4H_{10} and Ge_4H_{10} compounds shown in the top left are used to synthesize individual component layers (bottom left), which are then combined into seamlessly matched stacks (bottom right), culminating in an integrated device architecture with desired operational properties.

performance low-cost devices such as multijunction photovoltaics.

Most recently, it was shown that alloys with Sn concentrations below ~2% could be fabricated by replacing the exotic SiH_3GeH_3 precursor with commercially available Ge_2H_6 and Si_3H_8 sources, which enabled the development of micrometer thick films with reproducible control of atomic content and dopant densities directly on Si and Ge substrates.[7,11−13] Materials in this limited composition range (%Sn < 2) were then used to fabricate rudimentary *p*−*n* junctions that exhibited promising collection efficiencies approaching 80%.[7] This suggests that it may be possible to create working devices with tunable optical response beyond that of Ge by expanding the Sn content in the alloy without resorting to the use of Si_3H_8/Ge_2H_6 mixtures or the problematic SiH_3GeH_3. These limitations, and in particular the lack of flexible delivery agents for Si and Ge constituents, have therefore prevented the exploration of the full potential of the ternary $Ge_{1-x-y}Si_xSn_y$ system as a viable semiconductor for widespread device applications.

In this Article, we report a comprehensive study of a new molecular strategy that allows synthesis of device quality group IV Si−Ge−Sn semiconductors with demonstrated optoelectronic capabilities well beyond those of state-of-the-art Ge-based devices.[14] We have shown that the lower-reactivity Si_3H_8/Ge_2H_6 mixtures, which have so far limited the Sn incorporation, can be replaced by higher reactivity Si_4H_{10} and Ge_4H_{10} molecules. The latter are also more chemically compatible with Sn hydrides such as SnD_4 and react at unprecedented low temperatures of 285−320 °C to produce the next generation of $Ge_{1-x-y}Si_xSn_y$ alloys possessing the range of Si/Sn composition (up to 6% Sn and 22% Si) required for structure/property tuning. To exploit the enhanced reactivity of Si_4H_{10} and Ge_4H_{10} in the context of device development, we designed a custom single-wafer reactor operating under gas-source molecular beam epitaxy (GS-MBE) conditions, thereby enabling reproducible control of atomic content and thickness at the monolayer level, necessary for building quantum well-based structures. This approach also allows control and ultimately the elimination of secondary reactions responsible for introducing deleterious impurities into complex architectures of the grown devices, thereby diminishing their performance potential. A common example includes the incorporation of reactant residues from prior runs into subsequently grown components of the device (i.e., residual memory affects). In view of the novelty of the Si_4H_{10} and Ge_4H_{10} precursors for the growth of these crystalline semiconductors, we carried out ab initio thermochemistry studies to elucidate reactivity trends and identify optimal process conditions. These studies reveal a complex interplay between the equilibrium properties of the various reacting isomers at typical reaction conditions. Perhaps most importantly, we demonstrate that the crystalline $Ge_{1-x-y}Si_xSn_y$ systems grown using Si_4H_{10} and Ge_4H_{10} automatically lattice-match the underlying Ge wafers (the quintessential substrate for high efficiency PV) and that they possess defect-free microstructure, superior morphology, and viable thickness as needed for applications in multilayer devices. Furthermore, our approach offers the potential for additional improvements: (a) process scale-up to industry-standard large-area wafers, (b) improved efficiency and cost by using smaller amounts of expensive chemicals, (c) increased throughput by drastically reducing the down time due to chamber preparation for subsequent runs, and (d) simplified and consistent wafer cleaning.

In this Article, we describe the entire process development from "molecules through materials to prototype device" (see Figure 1) to produce intrinsic and doped functional components, which in turn allow the assembly of working photodiodes on Ge that exhibit the expected enhancements in optoelectronic performance. This is demonstrated by fabricating and measuring an entire series of photodetectors exhibiting record low dark current densities as compared to similar Ge-based devices grown on Si(100), as well as precisely tunable absorption edges over a broad energy range in the IR between 0.87 and 1.03 eV, thereby creating exciting opportunities in optoelectronics, including photovoltaics.

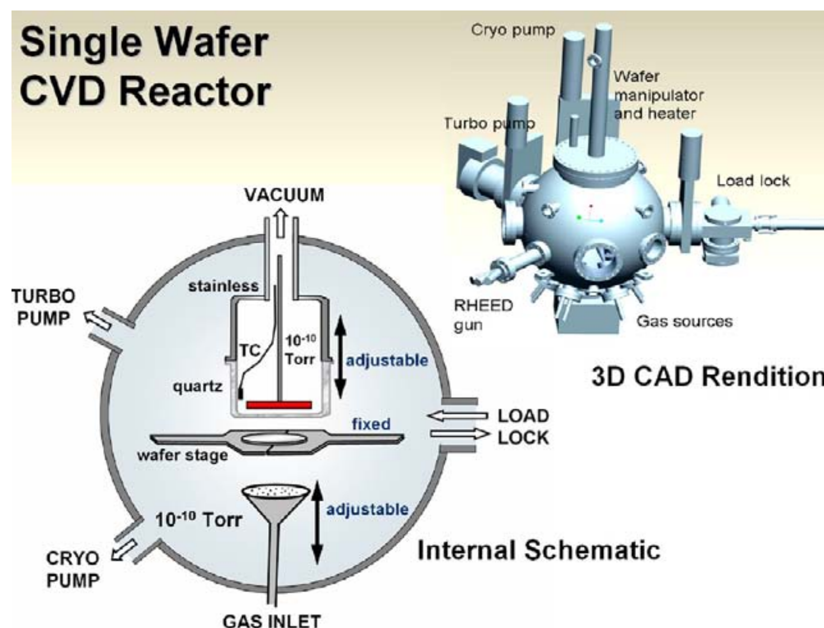

Figure 2. Schematic representations of the single wafer gas-source MBE reactor showing the internal structure of the CVD module, which includes the heater, wafer holder, and injection nozzle. A three-dimensional CAD rendering of the apparatus is shown in the inset.

II. RESULTS AND DISCUSSION

A. Growth and Structural Characterization. The growth apparatus used in this study (see Figure 2) is a custom-built deposition system with gas-source epitaxy capabilities in which a low-pressure CVD module (heater, wafer stage, gas injection manifold) is housed entirely within a UHV environment. The heater and sample stage are components of a single-wafer process unit that is attached to the top of a spherical stainless steel chamber. This chamber is fitted with a pumping stack comprised of high capacity turbo pumps backed by dry pumps. A cryo pump is used to maintain background vacuum levels of $\sim 10^{-10}$ Torr, which are necessary for "flashing" Si wafers to desorb the native oxide. The system is equipped with a load lock that allows transferring the substrate wafers into the chamber under UHV conditions. The sample stage comprises a rotating wafer holder designed to accommodate up to 4-in. substrates. Heating is provided by a coiled graphite element enclosed within a cylindrical quartz jar that is differentially pumped down to 10^{-10} Torr. This is a unique arrangement designed to: (1) isolate the heater from the reactor ambient for the purpose of protecting the filaments from the corrosive CVD environment, and (2) completely eliminate cross-contamination. The injection nozzle is mounted at the bottom of the chamber through a leak valve, and it is directed upward toward the wafer surface. The nozzle is terminated with a showerhead configured to dispense the gaseous reactants substantially normal to the downward facing wafer positioned upside down in the holder. The gas manifold is movable over an 8 in. length scale in the vertical direction, allowing the outlet of the nozzle to be precisely positioned below the wafer at a predetermined operating distance. The latter is optimized to produce films at the highest possible growth rate exhibiting thickness uniformities of 90% or better, depending on wafer size and temperature. The position of the quartz enclosure can also be adjusted in the vertical direction by a precisely controlled mechanism that is configured to independently set the distance between the heater and the back side of the wafer. The latter can be reduced to distance as little as 2 mm to ensure efficient and uniform radiant heating of the bulk substrate. Finally, the reactor is also fitted with in situ diagnostics, including a RHEED system to monitor bonding at the surface and a mass spectrometer (300 amu) to characterize the gaseous species present during growth and within the residual atmosphere at UHV conditions.

Using the above reactor, we initially conducted a series of control experiments on 4 in. diameter Si(100) and Ge(100) substrates. The Ge wafers employed here are those typically used as platforms in commercial multijunction photovoltaic devices, 150 μm-thick, off-cut by 6° toward (111), and doped with Ga acceptor atoms ($p = 6 \times 10^{17}$ cm^{-3}). Each "epi-ready" substrate was loaded as received in the reactor and then heated to 550 °C for 5 min under high vacuum to remove the surface oxide. In the case of the Si wafers, an RCA process was used to remove organic/metallic impurities. The substrates were then dipped in HF/methanol solutions to passivate the surface with hydrogen, loaded into the CVD chamber, and outgassed at 450 °C until the pressure was restored to the base level (10^{-10} Torr), and finally flashed at 850 °C to remove residual contaminants.

The Si_4H_{10} compound was obtained from Voltaix Corp. and was used as received. The Ge_4H_{10} analogue is produced by thermolysis of Ge_2H_6 in a flow system at 250 °C as described by the sequence of idealized equations below. The compound was isolated by distillation as a stable colorless liquid product in gram quantities sufficient for SiGeSn deposition studies.

$$2Ge_2H_6 \rightarrow Ge_3H_8 + GeH_4 \quad (1)$$

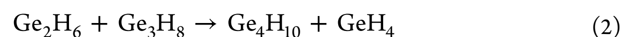

$$Ge_2H_6 + Ge_3H_8 \rightarrow Ge_4H_{10} + GeH_4 \quad (2)$$

Using ab initio thermochemistry (see below), we find that the driving force in these reactions is the creation of GeH_4, which is more easily produced by decomposition of Ge_3H_8 above 300 °C yielding Ge_4H_{10} (see eq 2). Stock gas mixtures were prepared by combining the Si_4H_{10}, Ge_4H_{10}, and SnD_4 precursors in a 3 L container. The molecular flux was admitted into the chamber at a steady flow rate, controlled by a precision

leak valve. A turbo pump (backed by a dry pump) was used to maintain a constant pressure of 1×10^{-4} Torr during growth, while the temperature of the samples was estimated from accurate readings (285−320 °C) of a heater thermocouple positioned inside a quartz enclosure, 5 mm removed from the backside of the wafer. Accordingly, the actual film temperatures are expected to be slightly lower. It should be noted that under the significantly reduced thermal budgets employed here the emissivity of Si and Ge is beyond the detection threshold of a single color pyrometer typically used to determine the substrate surface temperature.

A wide range of single-layer reference samples, both intrinsic and P-doped, was initially produced, on both Si(100) and Ge(100) substrates, for the purpose of establishing reliable and reproducible reaction conditions. The deposition temperature and molar ratio of the coreactants were optimized to ensure the growth of films with the desired compositions and dopant levels, while exhibiting large thicknesses, flat surfaces, and high-quality microstructure. Subsequently, all device-related developments were pursued exclusively on samples grown on Ge substrates. Using the optimized reference samples conditions, a range of device stacks of intrinsic and *n*-layers were then codeposited on off-cut Ge wafers to assemble $Ge_{1-x-y}Si_xSn_y$/Ge(100) *pin* diodes that were processed into photodetector devices. The intrinsic layers in these structures were synthesized by reactions of Si_4H_{10}, Ge_4H_{10}, and SnD_4 to yield nominal stoichiometries at unprecedented low temperatures as shown in Table 1. The *n*-type overlayer in each sample was grown under

Table 1. Compositions of Representative Samples Grown on Ge, and Processed into Photodetectors[a]

T (°C)	%Ge	%Si	%Sn
320	92.5	6.3	1.2
320	91.3	7.2	1.5
315	90.0	8.0	2.0
315	88.6	9.4	2.0
300	84.0	13.0	3.0
290	83.0	13.0	4.0
285	78.0	18.0	4.0
285	75.0	20.0	5.0

[a]The corresponding growth temperatures (first column) were obtained from thermocouple readings.

the same conditions in situ by introducing an appropriate amount of the single source $P(GeH_3)_3$ into the reaction mixture, to yield virtually identical Si, Ge, and Sn compositions and active dopant levels in the range of $2 \times 10^{19}/cm^3$. We found that the atomic content in the alloys was controlled by the relative amounts of the gaseous precursors in the reaction mixtures. The latter were formulated in a manner in which the amount of Ge_4H_{10} was always kept constant at 1.5 Torr per unit volume, which represents its maximum vapor pressure at 22 °C. The pressure of Si_4H_{10} and SnD_4 was then simultaneously adjusted to achieve an optimal ratio, which gave the target Si and Sn fraction in the layers reproducibly. Perhaps surprisingly, a significant excess of Si_4H_{10} was typically found necessary to systematically increase the alloy's Si concentration in the 6−20% Si regime of interest (ab initio thermochemistry is used to explore the origin of this behavior, see below). In all cases, the gas mixture was diluted with research grade H_2 at a total final pressure of 30−40 Torr, and checked prior to growth by gas infrared absorption, which confirmed that the individual components did not react or decompose even when stored for an extended period of time. The relative amount of H_2 in a given formulation did not influence the overall film stoichiometry, although higher diluents resulted in lower growth rates, as expected. The latter also depended on temperature and were estimated to be as high as 10 nm/min for the 315 °C depositions. Finally, we note that in the above list of samples in Table 1, the Si and Sn content is increased while keeping the Si/Sn ratio close to 3.7 for the purpose of tuning the band gap above that of Ge (0.8 eV), while maintaining the lattice parameter near that of germanium (5.658 Å). This ensures close lattice matching of the device stack with the underlying wafer.

All samples grown on Si(100) or Ge(100) (e.g., both reference layers and device stacks) were initially examined using Nomarski microscopy and found to be optically featureless. Rutherford backscattering spectroscopy (RBS), high-resolution X-ray diffraction (HR-XRD), atomic force microscopy (AFM), and cross-sectional electron microscopy (XTEM) characterization were then performed to establish that micrometer-thick films (single and double layers) could be readily produced with atomically flat surfaces.

Figure 3 shows the RBS random and aligned plots of a $Ge_{0.95}Si_{0.04}Sn_{0.010}$ reference sample deposited on Si(100) at 320

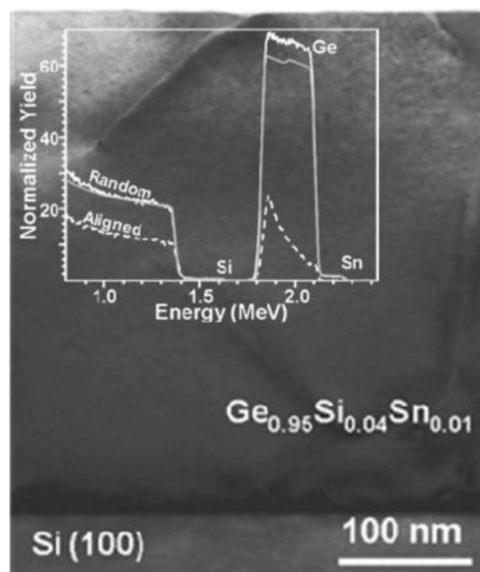

Figure 3. XTEM micrograph of a $Ge_{0.95}Si_{0.04}Sn_{0.01}$ layer grown directly on Si(100) and annealed at 700 °C showing the presence of defects resulting from the lattice mismatch of the epilayer with Si(100). (Inset) Random and channeled RBS spectra indicating a high level of epitaxial alignment and single phase structure of the epilayer.

°C with an Si/Sn ratio of ∼4. The data indicate single-phase material in full epitaxial registry with the underlying Si as shown by the high level of RBS channeling. The film is strain-free relative to Si(100) as indicated by the relaxation line passing through the center of the off axis (224) Bragg peaks (not shown). The corresponding XTEM image of the entire layer (Figure 3) shows occasional defects arising from the lattice mismatch between the epilayer and the substrate. In general, reference layers (or devices) grown on Ge under the same reactions conditions exhibited stoichiometry identical to those on Si, indicating that the ratio of coreactant on the growth front

controls the final composition irrespective of the growth platform employed.

Figure 4 shows typical RBS and XRD plots from a $Ge_{0.78}Si_{0.18}Sn_{0.04}$ device film as-grown on Ge at 310 °C with a thickness of ~750 nm. The random RBS plot (red trace) is used to determine the composition and estimate the thickness, while the channeled analogue (blue trace) indicates single-phase monocrystalline material grown with epitaxial alignment on the underlying wafer. The RBS analyses reveal a uniform Si/Sn content throughout the films with a margin of error of 0.1% Sn and 1% Si. The larger uncertainly in the Si fraction is due to the overlap of the Si signal with the dominant Ge wafer background, precluding a precise fit of the Si step height in the spectrum using the program RUMP.[15] In this case, XRD measurements were employed to confirm the Si content using the measured lattice constant of the epilayer in conjunction with Vegard's Law. The $2\theta/\omega$ plots and (224) reciprocal space maps typically contain a single Bragg reflection in each case corresponding to overlapping contributions from the intrinsic and *n*-type overlayers. However, we find that even a minor deviation in Si between the two layers of the device (not detectable by RBS) is manifested by a slight separation of their XRD peak maxima, as expected due to the highly resolved spectral features, as shown in Figure 4. In this sample, the (004) reflection of the *n*-$Ge_{0.78}Si_{0.18}Sn_{0.04}$ epilayer appears as a shoulder on the combined peak due to the Ge wafer and *i*-$Ge_{0.78}Si_{0.18}Sn_{0.04}$ epilayer. This indicates the expected reduction in lattice parameter due to intentional enhancement in Si content for the purpose of creating a higher bandgap capping layer, to optimize overall device performance. Perhaps most importantly, the width of the "device" peak is similar to that of bulk Ge, indicating minimal mosaic spread and flawless heteroepitaxial alignment, which is further corroborated by the presence of thickness fringe patterns on both sides of these $2\theta/\omega$ features. Collectively the XRD plots indicate superior crystallinity in the as-grown material and close similarity in the lattice constants to those of Ge (a_0 = 5.658 Å), as evidenced by a close correspondence of the epilayer and substrate peak maxima. These results are a testament to the precise nanoscale control of both stoichiometry and microstructure afforded by our ultralow temperature synthesis using designer hydrides with compatible reactivities.

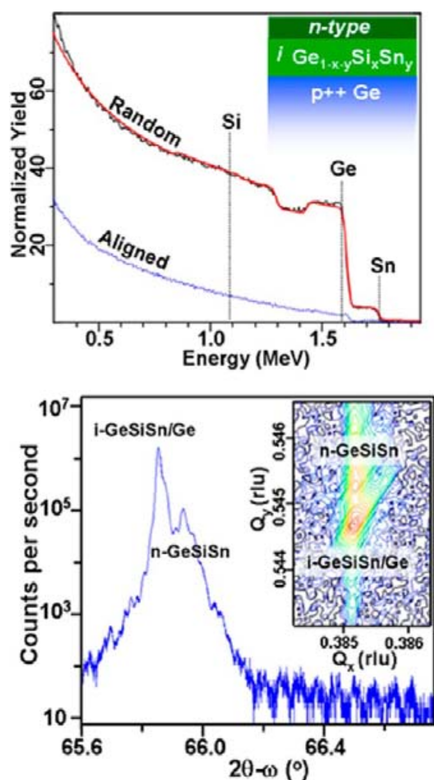

Figure 4. (Top) Standard 2 MeV RBS spectra of a 750 nm thick $Ge_{0.78}Si_{0.18}Sn_{0.04}$ epilayer illustrating a high degree of crystallographic alignment with the Ge wafer. (Bottom) XRD $2\theta/\omega$ plot of the same sample showing a strong (004) peak due to overlapping contributions from the Ge wafer and *i*-GeSiSn components of the device as well as a weak shoulder attributed to the *n*-GeSiSn overlayer. (inset) The (224) reciprocal space map due to *i*-GeSiSn/Ge(100) is perfectly aligned in the vertical direction with that of the *n*-GeSiSn overlayer. Collectively the XRD data reveal a very close degree of lattice matching and similar crystalline quality between the device structure and the Ge platform.

Secondary ion mass spectrometry (SIMS) depth profiles of selected samples showed a homogeneous distribution of the Si, Ge, and Sn atoms. The plots also revealed a sharp transition in the P profile across the heterojunctions, reaching a constant value of $\sim 2 \times 10^{19}/cm^3$ within the top layer. AFM scans revealed a root-mean-square (RMS) roughness of ~ less than 0.7 nm for 20×20 μm^2 areas in samples across the entire composition series, indicating a homogeneously smooth surface in all cases. The latter is corroborated by XTEM observations, which revealed the presence of monocrystalline layers with atomically flat surfaces and cubic diamond-like structures akin to that of the underlying Ge platform, as illustrated in Figure 5 by micrographs of two representative GeSiSn/Ge *pin* samples. The top and bottom panels of the figure are diffraction contrast images obtained from 3% and 5% Sn films, respectively, both showing a flat surface and uniform layer morphology with typical thickness variations appearing as alternating bright and dark contrast bands. In both cases, the entire layer is found to be completely devoid of threading dislocations on a lateral scale of many micrometers. Virtually identical defect-free microstructures are observed by XTEM within full layer segments throughout the cross-sectional samples. The middle panel of the figure is a high-resolution image of the $Ge_{0.75}Si_{0.20}Sn_{0.05}$/Ge(100) interface region showing a sloped heterojunction profile (indicated by arrows) relative to the (111) planes, as expected from the off-cut wafer geometry. The overlayer is fully conformal to the underlying terraced surface of the wafer, while the two materials exhibit a flawless epitaxial registry due to close lattice matching.

B. Reactivity Studies of the Ge_4H_{10} and Si_4H_{10} Precursors. The SiGeSn films with 1−5% Sn compositions described above are specifically targeted to lattice match Ge by maintaining a ratio of Si/Sn ~ 3.7, while the corresponding Si/Ge ratios vary systematically from about 4−27%. In these depositions, the latter ratio is controlled by adjusting the partial pressures of the Si and Ge molecular precursor sources. We find that a considerable excess of Si_4H_{10} as compared to Ge_4H_{10} is needed to incorporate target levels of silicon into the growing films in the range of 4−20%. For instance, maintaining a partial pressure ratio of 2:1 between the Si_4H_{10} and Ge_4H_{10} at 300 °C in the gas-phase reactant mixture yields a sample containing 12% Si and 85% Ge. This suggests that the Si_4H_{10} and Ge_4H_{10} possess dramatically different reactivities. In the case of Ge_4H_{10}, some insight into its reactive behavior was provided by our prior work in which this compound was used as the source in

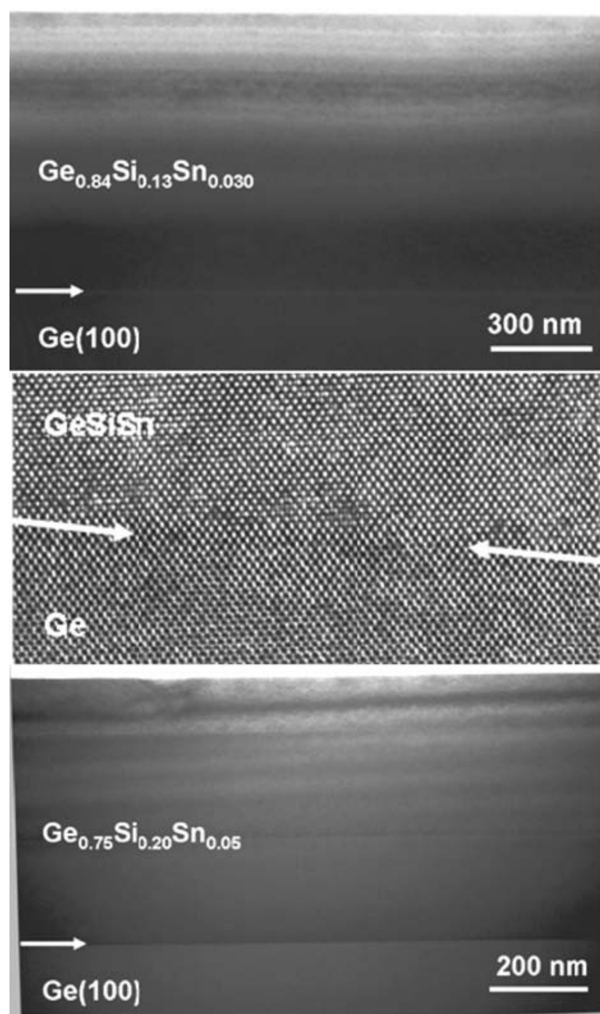

Figure 5. XTEM micrographs of *p*−*i*−*n* device structures with nominal compositions of $Ge_{0.84}Si_{0.13}Sn_{0.03}$/Ge (top panel) and $Ge_{0.75}Si_{0.20}Sn_{0.05}$/Ge (bottom panel) as grown at 300 and 290 °C, respectively. The layers in both cases possess defect-free microstructures, flat surfaces, and viable thicknesses up to 1 μm as needed for applications in multilayer devices. High-resolution image (middle panel) of the sloped heterointerface marked by arrows indicating highly conformal and fully commensurate growth of the $Ge_{0.75}Si_{0.20}Sn_{0.05}$ device on the off-cut Ge wafer.

ultralow temperature growth of Ge films.[16] There we showed, using state-of-the-art first principles thermochemistry simulations, that iso-Ge_4H_{10} is the dominant isomer, as compared to the "normal" (*n*) and "gauche" (*g*) analogues, at typical synthesis conditions similar to those used in the present work. The isomeric speciation predicted theoretically was corroborated by measured gas-phase FTIR spectra of the compound, whose main features are very well accounted for using the weighted sum of the theoretically calculated isomeric spectra.

One of the outcomes of equilibrium thermodynamic and reactivity studies of the Ge_4H_{10} isomers is that the iso-Ge_4H_{10} compound plays a key role in the film deposition. This notion is supported by the isotropic character of its molecular structure and the presence of the highly reactive −Ge−H moiety (tertiary site), which represents a facile mechanism for binding the molecule onto the Ge (or Si) substrate surface. The resulting −Ge(100)−Ge−$(GeH_3)_3$ intermediate is then completely analogous to that proposed[17] in the reaction of neopentasilane, $Si(SiH_3)_4$, on silicon to form −Si(100)−Si−$(SiH_3)_3$ via elimination of SiH_4. In view of this analogy, and even conceding the existence of a small reactivity difference of iso-Si_4H_{10} and iso-Ge_4H_{10} on a Ge(100) surface (due to the slightly stronger Si−H bonds), the requirement of a large excess of the Si_4H_{10} source in our film growth is difficult to explain. At the low deposition pressures mentioned above (10^{-4} Torr), gas-phase reactions between the Si_4H_{10} and Ge_4H_{10} sources are likely to be negligible. Thus, the required Si_4H_{10} excess must be explained by the equilibrium thermodynamics of the reactant isomers present at the growth front. For example, a large concentration of the *n*-Si_4H_{10} and *g*-Si_4H_{10} isomers with reduced reactivities over the *i*-Si_4H_{10} might explain the need for large excess of Si_4H_{10} to produce the desired alloy compositions.

To examine our conjecture on a more robust footing, we pursed a targeted, and comparative, first principles thermochemistry study of Si_4H_{10} and its isomers to determine their proportions at growth conditions. For consistency, and to facilitate straightforward comparisons with our prior work on the related Ge_4H_{10} molecules,[16] we here adopt the same quantum simulation methods and theoretical thermochemistry procedures. Specifically, all of our calculations are based on density functional theory (DFT) as implemented in the Gaussian 03 code,[18] using the B3LYP hybrid exchange-correlation functional in conjunction with a standard 6-311G ++(3df,3pd) basis set. All static molecular ground-state structures (see Table 2) were converged using an RMS force criterion of 10^{-6} (designated using the "VeryTight" keyword in Gaussian 03), "ultrafine" integration grids (75 radial shells and 203 angular points per atom), and no symmetry constraints imposed during optimization. In all cases, the harmonic normal-mode frequencies calculated for the ground state molecular structures are found to be positive definite, indicating that the molecules are dynamically stable. A symmetry analysis of our final converged structures yielded C_{3v}, C_{2h}, and C_2 point groups for the *i*-Si_4H_{10}, *n*-Si_4H_{10}, and *g*-Si_4H_{10} molecules, respectively, which are identical to those obtained for the corresponding Ge_4H_{10} species.[16]

As in the case of the Ge_4H_{10}, the Si_4H_{10} bond lengths calculated from our simulations are in general excellent agreement with those obtained by other authors, and in our prior work and follow expected trends.[19,20] The shortest Si−Si bond lengths (2.351 Å) typically occur between $-SiH_3$ and $-SiH_2-$ moieties, while slightly longer values (2.355 Å) are found between $-SiH_3$ and −SiH−, or adjoining $-SiH_2-$ groups. In analogy with the Ge analogue, the Si−H bond lengths are also found to follow the expected increasing trend 1.483, 1.486, and 1.490 Å for the $-SiH_3$, $-SiH_2-$, and −SiH− moieties, respectively. The bond angle trends in these molecules also exhibit systematic patterns with typical ∠Si−Si−Si angles of ∼113° among the isomers having a branched character, but a more tetrahedral value of 110.9° in the case of the *i*-Si_4H_{10} species possessing C_{3v} symmetry. The torsion angle among the Si atoms adopts trivial values for the high symmetry species and a value of 65° for the *g*-Si_4H_{10} isomer, close to the typical 63° value found in the gauche isomer of butane. We note here that a smaller value of 58° was found in our simulation of the corresponding *g*-Ge_4H_{10} isomer.[16] The dipole moments of the isomers (listed in Table 2) indicate a maximum value of 0.105 D for the *i*-Si_4H_{10} molecule, 0.06 D for *g*-Si_4H_{10}, and a vanishing dipole moment for the *n*-Si_4H_{10}, as expected.

Table 2. Summary of Structural and Energetic Results for the Three Si_4H_{10} Isomers[a]

		iso-tetrasilane (i-Si_4H_{10})	n-tetrasilane (n-Si_4H_{10})	g-tetrasilane (g-Si_4H_{10})
point group		C_{3v}	C_{2h}	C_2
bond lengths (Å)	Si−Si	2.353	2.351(×2), 2.354	2.351(×2), 2.355
	$(Si-H)_T$	1.483(×9)	1.483(×3)	1.483(×3)
	$(Si-H)_S$	1.490*	1.486	1.486
bond angles (deg)	∠Si−Si−Si	110.9	112.6	112.9
	$(H-Si-H)_T$	108.5(×2), 108.6	108.5, 108.6(×2)	108.5, 108.6(×2)
	$(H-Si-H)_S$		107.5	107.6
dipole moment (D)		0.1046	0.0000	0.0591
thermochemistry	E_0 (au)	−1164.10846	−1164.10750	−1164.10690
(T = 298 K, P = 1 atm)	$E_0 + E_{th}$ (au)	−1164.01457	−1164.01383	−1164.01329
	$E_0 + H_{th}$ (au)	−1164.01363	−1164.01288	−1164.01235
	$E_0 + G_{th}$ (au)	−1164.05994	−1164.05935	−1164.05907
	S (cal/(mol K))	97.5	97.8	98.3

[a]The subscripts "T" and "S" refer to terminal and sagittal H−Si−H bond angle species. The asterisk on the $(Si-H)_S$ bond length in i-Si_4H_{10} indicates that the −Si−H moiety is distinct from the other sagittal $-SiH_2-$ moieties. Note: Thermochemistry functions in this table are not corrected for internal rotor contributions.

The standard thermochemistry output from Gaussian 03 at T = 298 K and P = 1 atm is also summarized in Table 2 and includes the static electronic energy of the Si_4H_{10} isomers (E_0), as well as its thermally corrected counterparts for internal energy (E_{th}), enthalpy (H_{th}), and free energy (G_{th}). In analogy with the results for the Ge_4H_{10} isomers[16] the i-Si_4H_{10} species possessing C_{3v} symmetry is found to have the lowest energies (E_0, $E_0 + E_{th}$, $E_0 + H_{th}$, and $E_0 + G_{th}$), followed by the corresponding higher energies of n-Si_4H_{10} and g-Si_4H_{10}. The distinctions and similarities in the free-energy trends of the Ge_4H_{10} and Si_4H_{10} isomers are summarized in Figure 6, where

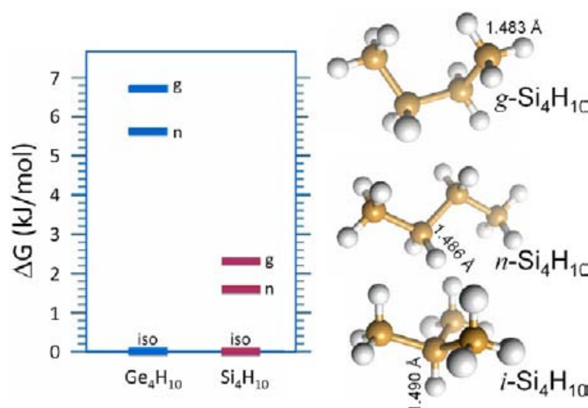

Figure 6. (Left panel) Relative Gibbs free energies of Ge_4H_{10} and Si_4H_{10} isomers, indicating a common ordering on the energy scale but much smaller energy differences among the Si-based isomers. (Right panel) Molecular structures of the Si_4H_{10} isomers. The calculated Si−H bond lengths shown indicate a systematic dilation from the $-SiH_3$ to $-SiH_2$, to −SiH, implying that the latter is likely the most thermally labile.

the i-Si_4H_{10} values are used as a reference (Ge_4H_{10} values taken from ref 16). The most notable distinction between the relative free energies of the Ge_4H_{10} isomers, and their Si counterparts, is the dramatically reduced energy separation in the latter, which is comparable to k_BT at 300 K (∼2.5 kJ/mol). This implies that the iso-, n-, and g-Si_4H_{10} mixture should be roughly equimolar at room temperature. Finally, Table 2 lists the molecular entropies of the Si_4H_{10} isomers obtained at T = 298 K, which are found to be virtually independent of the isomer species, in contrast to the Ge_4H_{10} case, in which the largest entropy was obtained for the n-Ge_4H_{10} isomer, due to its larger moment of inertia. An analysis of the rotational and vibrational contributions indicates that the total entropies are controlled by rotations in Si_4H_{10} and vibrations in Ge_4H_{10}. Ultimately, as discussed below, the playoff in the temperature dependence of the vibrational and rotational contributions to the free energy leads to manifestly different thermodynamic behavior in Si_4H_{10} and Ge_4H_{10} isomers.

The isomeric mixture in Si_4H_{10} is comprised of linear and gauche conformational isomers (n-Si_4H_{10} and g-Si_4H_{10}) and the positional isomer i-Si_4H_{10}, which is predicted to possess the smallest free energy. In our earlier studies of butane-like Si−Ge hydride isomeric mixtures,[21] we introduced the concept of fitting a linear combination of calculated isomeric vibrational spectra to the experimental spectrum of a mixture, to ascertain the relative proportions in the experimental gas-phase mixture. Here, instead we apply an ab initio thermodynamic approach based on free-energy minimization for the three isomerization reactions:

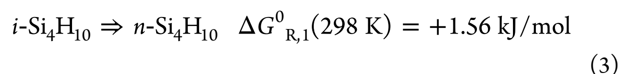

$$i\text{-}Si_4H_{10} \Rightarrow n\text{-}Si_4H_{10} \quad \Delta G^0_{R,1}(298\ K) = +1.56\ kJ/mol \tag{3}$$

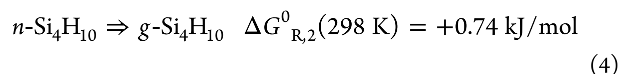

$$n\text{-}Si_4H_{10} \Rightarrow g\text{-}Si_4H_{10} \quad \Delta G^0_{R,2}(298\ K) = +0.74\ kJ/mol \tag{4}$$

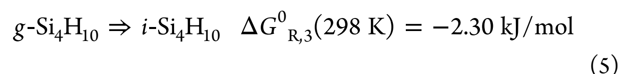

$$g\text{-}Si_4H_{10} \Rightarrow i\text{-}Si_4H_{10} \quad \Delta G^0_{R,3}(298\ K) = -2.30\ kJ/mol \tag{5}$$

where the reaction free energies are obtained directly from the $E_0 + G_{th}$ data listed in Table 2. All thermodynamic functions were obtained assuming ideal gas behavior and mixing, and the neglect of possible internal rotor contributions. The automatically generated analysis of the latter corrections provided by Gaussian 03 for these molecules (and Ge_4H_{10} analogues) identified the related normal modes as involving torsions in the molecular backbone, and rotations of the terminal $-SiH_3$ groups. Typical corrections to the thermal energy are estimated to be on the order of ∼0.1−0.2 kJ/mol at ∼300 K, and we note that in the present system similar rotor contributions appear on both sides of the reactions listed above (eqs 3−5), suggesting a significant cancellation of error. Accordingly, our analysis below neglects these rotational corrections.

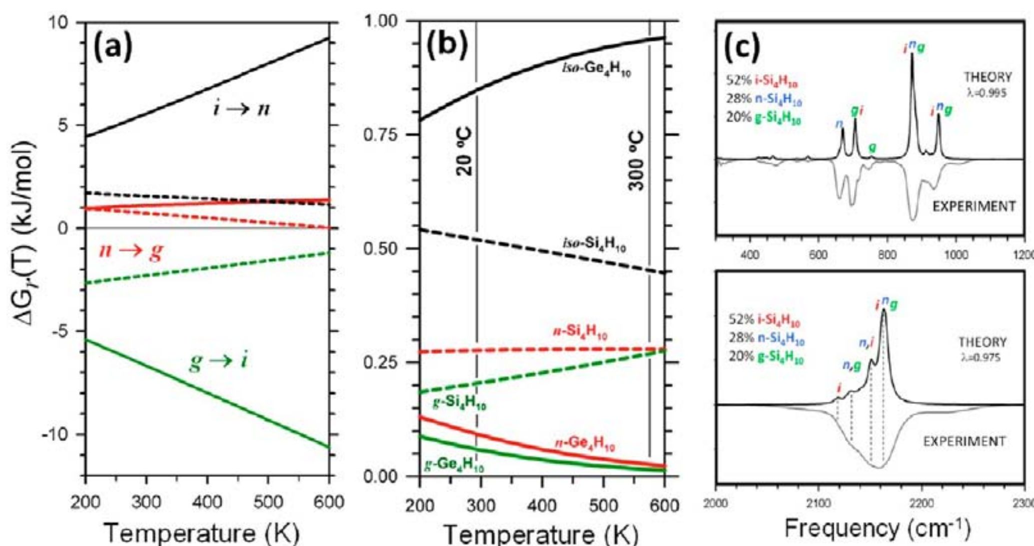

Figure 7. (a) Calculated temperature dependence of the Si_4H_{10} (dashed lines) and Ge_4H_{10} (solid lines) isomer reaction free energies up to 600 K, and (b) that of the resulting equilibrium mole fractions predicted for both Si_4H_{10} and Ge_4H_{10} isomers. Note the predominance of iso Ge_4H_{10} at 300 °C as compared to a nearly equimolar distribution in Si_4H_{10}. (c) Composite room temperature IR spectrum of Si_4H_{10} obtained by linearly combining the calculated IR spectra of its isomers according to the predicted equilibrium mixture. Scale factors of 0.995 and 0.975 were applied to the calculated spectra in the low- and high-frequency regimes, respectively. Theoretical and experimental spectra are oriented upward and downward, respectively, as indicated within the plots in part (c).

The temperature-dependent equilibrium mixture is described by a simple system of (cyclic) coupled equations, described in detail in ref 16. At 298 K, the equilibrium constants obtained from the free energies listed in Table 2 are $K^0_{P,1} = 0.5329$, $K^0_{P,2} = 0.7425$, and $K^0_{P,3} = 2.5274$ yielding isomer mole fractions n_i = 52%, n_n = 28%, and n_g = 20%. This roughly equimolar distribution of the Si_4H_{10} isomers is dramatically distinct from the results obtained for Ge_4H_{10}[16] in which the same computational methods and procedures yielded n_i = 85%, n_n = 9%, and n_g = 6%. This dichotomy can be traced to the small calculated free-energy differences among the Si_4H_{10} isomers, in comparison to their Ge_4H_{10} counterparts. Additional insight is afforded by examining the temperature dependence of the reaction free energies, which is obtained here by re-evaluating the thermochemistry for reactions 3−5 over the appropriate range of 200−600 K, because this includes our deposition conditions of 285−320 °C. The resulting thermodynamic behavior is summarized Figure 7, which shows plots of the isomerization reaction free energies for Si_4H_{10} as well the corresponding results for Ge_4H_{10} (taken from ref 16). We note in Figure 7b that while ordering in the reaction free energies for both Si_4H_{10} and Ge_4H_{10} is qualitatively the same ($\Delta G_r[i \rightarrow n] > \Delta G_r[n \rightarrow g] > \Delta G_r[n \rightarrow g]$) over the indicated temperature range, their rates of change with temperature are typically opposite in sign (where the Ge species increase the Si decreases and vice versa). In particular, the model predicts that at the growth conditions, an equimolar mixture of Si_4H_{10} and Ge_4H_{10} contains twice as much of the reactive *i*-Ge_4H_{10} isomer in proportion to its *i*-Si_4H_{10} counterpart. This reduction in the availability of the most reactive Si source may partially account for the observed excess in Si_4H_{10} needed to achieve the desired GeSiSn film compositions.

To validate the simple thermodynamic model above, we next attempt to reproduce the observed room temperature IR spectrum of Si_4H_{10} by combining the calculated spectra of *i*-Si_4H_{10}, *n*-Si_4H_{10}, and *g*-Si_4H_{10} in the 52%, 28%, and 20% proportions predicted by the equilibrium calculation above. As shown in Figure 7c, where the theoretical and experimental spectra are oriented upward and downward, respectively, the plots indicate that the equilibrium molar fractions account well for the principal character (frequencies and intensities) of the corresponding experimental spectrum. Most importantly, and in contrast to Ge_4H_{10},[16] we find that the observed spectrum cannot be accounted for theoretically using any individual isomer spectrum alone. Changes in the proportions of as little as ∼5% among the isomeric contributions produces large discrepancies in the intensity ratios between the calculated and experimental spectra. In the case of Si_4H_{10}, several of the low-frequency features (<800 cm^{-1}) in the IR spectrum can be clearly assigned to a specific isomer, as indicated in the plots using the designations "*i*", "*n*", and "*g*". On the other hand, the most intense vibrations (∼870 cm^{-1}) exhibit almost the same (common) frequency in all three isomer gas-phase species.

C. Device Fabrication and *I*−*V* Characteristics. Photodiodes were fabricated with compositions listed in Table 1 using previously developed procedures for related GeSn IR devices.[22,23] The above were processed as-grown with no further thermal treatments as typically employed by previous workers to improve defect microstructure in related materials.[22] Devices are produced in a circular mesa geometry by etching the surrounding material down to the *p*-type Ge wafer (∼3 × 10^{17}/cm^3). The top and bottom metal contacts consist of annular Cr/Au layers with thickness of 20/200 nm. A 100 nm-thick SiO_2 coating is first deposited. The mesas are then patterned via photolithography and etched by reactive ion plasma using BCl_3. They are subsequently passivated with a 100 nm-thick SiO_2 antireflective coating deposited by plasma-enhanced CVD (PECVD). Metal contact pads are then defined using the AZ5214 resist, and the samples are baked at 115 °C for 90 s to facilitate metal lift-off. The SiO_2 layer in the contact areas is removed by a buffered oxide etchant, and the metals are deposited via e-beam evaporation. The formation of electrical pads is finalized by lift-off in acetone, and the resultant devices are finally cleaned in an oxygen plasma.

Current−voltage ($I-V$) measurements were performed on mesas with diameters 100, 200, 300, 500, and 1000 μm, and their respective dark currents were determined at a nominal bias of −1 V. Figure 8 (top) shows representative $I-V$ plots for a $Ge_{0.925}Si_{0.063}Sn_{0.012}$ sample indicating remarkably low dark current densities of ∼1 × 10^{-3} J(A/cm^2), which are essentially independent of the device size. Figure 8 (bottom) compares a representative set of current densities as a function of concentration. The magnitudes of the dark currents in this case very slightly increase from 1 × 10^{-3} to 2 × 10^{-3} J(A/cm^2) with Si/Sn content. Alloy devices with 1−2% Sn content exhibit lower ideality factors at n = 1.1−1.2 than 3−5% analogues, which show values in the n = 1.3−1.4 range.

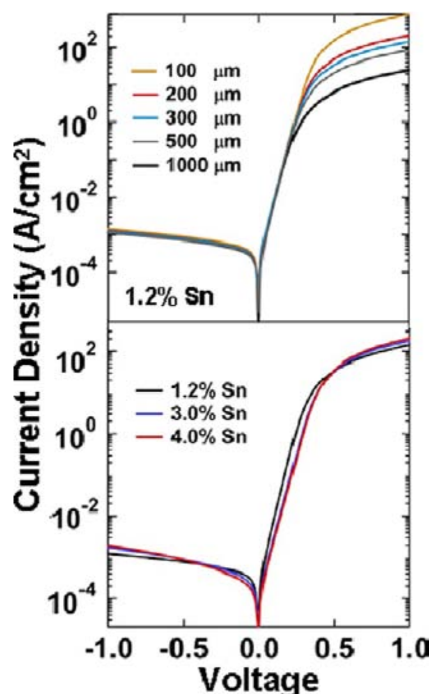

Figure 8. Current density curves for GeSiSn photodiodes. Top panel shows the plots of a $Ge_{0.925}Si_{0.063}Sn_{0.012}$, devices with diameters ranging from 100 to 1000 μm. The bottom panel compares the curves obtained from selected samples measured from 300 μm mesas, indicating lower dark currents relative to Ge on Si devices with similar geometries.[22]

We note that the above device dark currents are much lower than those of Ge and GeSn on Si(100) counterparts by at least an order of magnitude.[22] They are also reduced from those observed in our Sn-doped Ge materials and diluted $Ge_{1-y}Sn_y$ alloys [5 × 10^{-2} J(A/cm^2)].[23] The lower dark current in GeSiSn can be attributed to its higher fundamental band gap, the structural perfection of the film/substrate interface, and the superior crystal quality. In the case of Ge or GeSn grown on Si(100), the lattice mismatch produces misfit dislocations of which some cores propagate into the bulk layer as deleterious threading defects. This effect seems to be removed in the ternary system, in which lattice matching between the GeSiSn and the underlying Ge can be readily achieved for Si/Sn ratios in the vicinity of 3.7.

Arrhenius plots of the dark current densities as a function of temperature were used to estimate their activation energies for a series of voltage measurements conducted between 0.5 and 2.0 V. The data for a $Ge_{0.925}Si_{0.063}Sn_{0.012}$ device are illustrated in Figure 9, which shows that for the above bias range these energies span from 0.578 to 0.478 eV, respectively. The low-

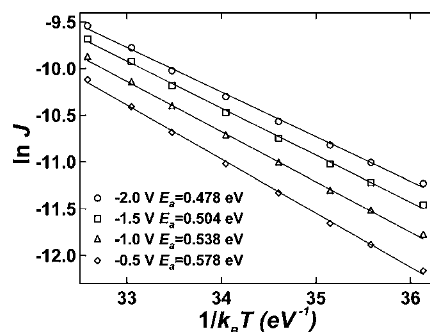

Figure 9. Arrhenius plots of the dark current densities at selected reverse bias values for the $Ge_{0.925}Si_{0.063}Sn_{0.012}$/Ge diode. The activation energies are obtained from the slopes of the lines.

voltage value is significantly higher than $E_g/2$, where E_g is the fundamental band gap for this alloy, estimated to be close to ∼0.70 eV following the procedure described in ref 7. The corresponding activation energies at −0.5 V for $Ge_{0.913}Si_{0.072}Sn_{0.015}$, $Ge_{0.886}Si_{0.094}Sn_{0.02}$, $Ge_{0.84}Si_{0.13}Sn_{0.030}$, $Ge_{0.78}Si_{0.18}Sn_{0.04}$, and $Ge_{0.75}Si_{0.20}Sn_{0.05}$ are found to be 0.524, 0.557, 0.524, 0.493, and 0.486 eV, respectively, which are also higher that the expected values of $E_g/2$ for these. These results suggest that the dark current is not completely dominated by Schottky−Read−Hall recombination but has a significant diffusion component as well, underscoring the high crystal quality of the ternary alloy layers in all samples studied to date, regardless of composition and intrinsic layer thickness.

D. Optical Response and Direct Gap Determination. The spectral response of the fabricated devices was measured using monochromatized light originating from a tungsten halogen lamp. The light was modulated with a mechanical chopper and then transmitted onto the SiO_2 diode window using an optical fiber equipped with a focusing lens whose spot size (30 μm) is significantly smaller than all measured devices. The resultant photocurrent induces a voltage on a 100 Ω resistor that was measured by a lock-in amplifier. The voltage and resistance were then used to calculate the photocurrent, which was divided by the power of the incident light to obtain the responsivity R.

Figure 10 shows the spectral dependence of the external quantum efficiency (EQE) of a $Ge_{0.78}Si_{0.18}Sn_{0.04}$ sample measured from a device 300 μm in diameter at 0.0 V bias [EQE = 1240 nm × R/λ (nm)]. The two absorption edges at 1590 nm (0.78 eV) and 1230 nm (1.02 eV) nm are assigned to direct-gap absorption in the Ge substrate and alloy epilayer, respectively (the direct gap E_0 in bulk, intrinsic Ge is at 0.805 eV at room temperature; the small downshift in our sample is due to band gap renormalization in the highly doped Ge wafer). The significant photoresponse observed in this case is attributed to the improved crystallinity of the material grown directly on bulk Ge under pseudo homoepitaxy conditions. The signal of the plot is significantly reduced beyond 1600 nm because only indirect absorption in Ge can contribute to the photocurrent. The EQE becomes essentially zero at 1800 nm, near the fundamental Ge band gap.

Figure 11 shows EQE versus wavelength plots comparing the optical response of photodiodes containing ∼1−4% Sn. The plots were derived from photocurrent measurements made on

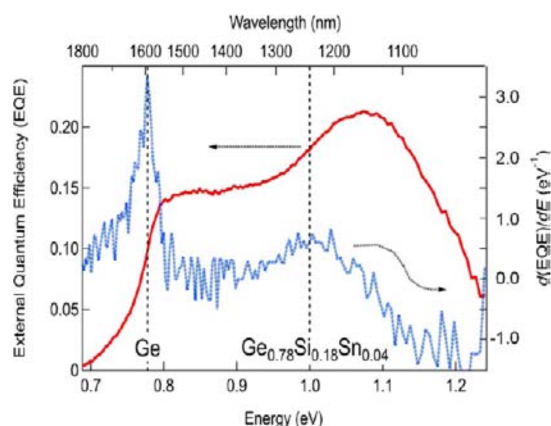

Figure 10. External quantum efficiency (EQE) and its derivative (red and blue curves, respectively) as a function of energy for a heterostructure diode with composition $Ge_{0.78}Si_{0.18}Sn_{0.04}$ measured at zero bias. The data show the absorption edges for the Ge substrate at 1580 nm and the epilayer at 1230 nm. The vertical lines indicate the position of the direct gap, determined as discussed in the text.

devices with mesa size 300 μm in diameter at 0.0 V bias. The peak maxima were normalized to facilitate comparisons of the responsivity among devices with varying active layer thickness from 0.5 to 1 μm depending on composition. The Ge wafer photoresponse is not shown here to emphasize minor shifts of the absorption peaks as a function of alloy composition. In general, the plots show that the simultaneous increase of Sn (1−4%) and Si (6−18%) while keeping the Si/Sn ratio at 4 ± 1 produces a systematic and significant shift of the absorption wavelength by ~200 nm within this range. For example, in the case of the $Ge_{0.925}Si_{0.063}Sn_{0.012}$ and $Ge_{0.913}Si_{0.072}Sn_{0.015}$ samples, their absorption edges (at left panel) are clearly resolved given the very slight difference in their respective stoichiometries, providing unequivocal evidence that the simultaneous incorporation of Si and Sn produces a measurable opening of the band gap. In contrast, the plots for samples $Ge_{0.84}Si_{0.13}Sn_{0.03}$ and $Ge_{0.83}Si_{0.13}Sn_{0.04}$ (at right panel) show that increasing the Sn at fixed Si content reduces the gap while keeping Sn constant and increasing Si leads to significant opening of the gap, as in the case for the $Ge_{0.78}Si_{0.18}Sn_{0.04}$ and $Ge_{0.83}Si_{0.13}Sn_{0.04}$ sample pair. In this regard, the latter effect is also observed for the $Ge_{0.900}Si_{0.08}Sn_{0.02}$ and $Ge_{0.886}Si_{0.094}Sn_{0.02}$ samples (left panel) in which a slight increase in Si (from 8% to ~10%) while keeping Sn constant (2%) produces the expected trend of decreasing wavelength. These findings indicate that small changes in the Sn content have a profound and systematic effect on the optoelectronic properties of the material and suggest that the tunability of the responsivity is highly precise, representing a powerful new design tool in the development of devices with targeted optoelectronic properties.

E. Direct Gap Dependence on Composition. In this work, we determined the direct band gap E_0 of the $Ge_{1-x-y}Si_xSn_y$ alloy using a simple procedure, which allows for a straightforward determination of the direct absorption threshold. We compute numerically the energy derivative of the EQE, and we fit the resulting line shape with a Gaussian. An example of the derivative spectrum is shown as a blue trace in Figure 10. We find that this method gives values of E_0 in excellent agreement with earlier ellipsometric determinations of the band gap.[24] The energies extracted from our derivative fits are corrected for minor residual strain effects using the measured strain from our X-ray data and deformation potentials from ref 6. The corrected values are shown (as ●) in Figure 12 as a function of the non-Ge fraction $X = x + y$. The strain shifts are very small, ranging from 2 meV to a maximum of 10 meV. In applying this correction, it is assumed that the absorption is dominated by transitions from the heavy-hole band. The systematic error associated with this assumption is estimated to be on the order of 1 meV. The error bars on the data in Figure 12 are mostly smaller than the size of the circles in the figure.

In earlier work, we wrote the compositional dependence of the E_0 gap in $Ge_{1-x-y}Si_xSn_y$ alloys as[6]

$$E_0(x, y) = E_0^{Ge}z + E_0^{Si}x + E_0^{Sn}y - b^{GeSi}xz - b^{GeSn}yz - b^{SiSn}xy \quad (6)$$

where $z = 1 - x - y$, E_0^{Ge}, E_0^{Si}, and E_0^{Sn} are the E_0 gaps in Ge, Si, and α-Sn, respectively, and the b's are the bowing parameters in the corresponding binary alloy systems. This expression

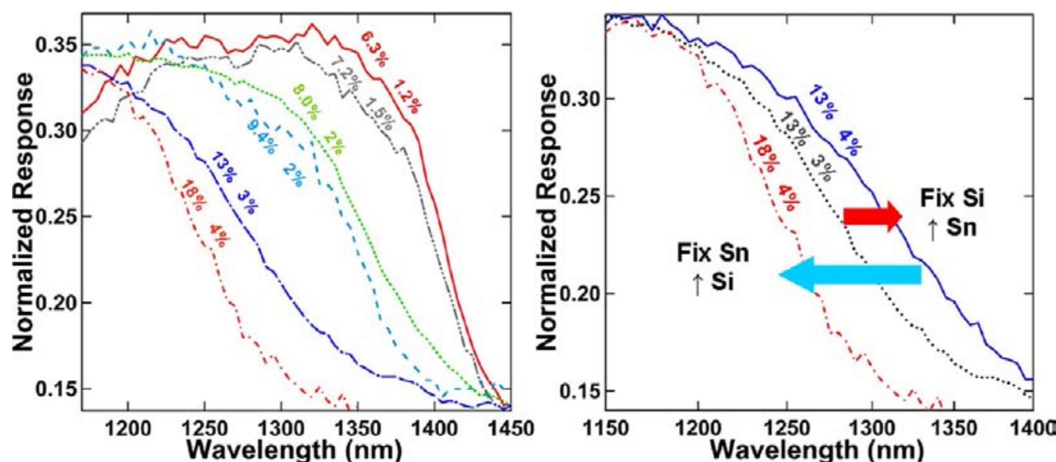

Figure 11. (left) Normalized responsivity versus wavelength plots of heterostructure diodes with Sn contents of 1−4% measured at zero bias. The absorption edge is found to shift to lower IR wavelengths by simultaneously increasing Sn and Si incorporation over a very narrow composition range. The % values on each curve refer to the Si and Sn contents, respectively. (right) EQE plots comparing the absorption edges of several selected GeSiSn samples in which increasing the Sn at fixed Si content reduces the gap while keeping Sn constant and increasing Si results in a significant opening of the gap.

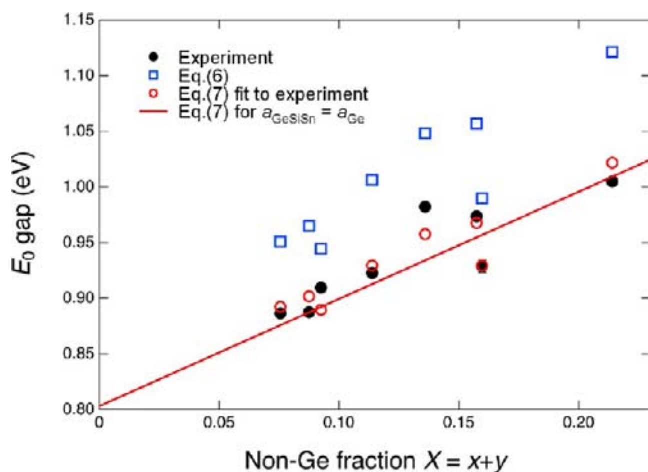

Figure 12. Direct gap E_0 energies in $Ge_{1-x-y}Si_xSn_y$ alloys as a function of the non-Ge fraction $X = x + y$. Solid black circles correspond to experimental data. The blue squares represent the prediction from eq 6. The red circles are the results from a bilinear (in x and y) fit of the experimental energies shown in eq 7. The red line is the prediction from eq 7 for the case of exact lattice match between GeSiSn and Ge.

neglects the contribution of ternary-specific terms in the polynomial expansion of the band gap energy, such as those proportional to xyz. Its validity can be tested experimentally by performing measurements in the three binary alloy systems. In our case, however, the $Si_{1-y}Sn_y$ alloy is very poorly known, and the compositional dependence of its E_0 gap has not been measured. Thus, eq 6 was fit to $Ge_{1-x-y}Si_xSn_y$ data in ref 24 using b^{SiSn} as an adjustable parameter, and it was shown that a reasonable good fit of the data was obtained using $b^{SiSn} = 13.2$ eV. The remaining parameters in eq 6 are known from work on binary alloys and elemental semiconductors,[25] and in Figure 12 we show as blue □ the resulting prediction using the above value for b^{SiSn} and $E_0^{Ge} = 0.803$ eV, $E_0^{Si} = 4.093$ eV, $E_0^{Sn} = -0.42$ eV, $b^{GeSn} = 2.2$ eV, and $b^{GeSi} = 0.21$ eV. We notice that the predicted energies follow the experimental trend quite well, but there is a systematic upward shift of about 75 meV with respect to the observed values (solid symbols). The discrepancy is due to the fact that in ref 24, eq 6 was fit to the data over a very broad range of compositions with $X < 0.6$, whereas in the present work the data points cover a much narrower range $0.06 < X < 0.2$. As indicated above, our new data (solid symbols in Figure 12) overlap very well with the ellipsometric data in ref 24 (not shown here) over the same compositional range, leading to the conclusion that the observed ~75 meV deviation is not a systematic error that can be attributed to the different experimental techniques used to measure E_0, but is rather a limitation of eq 6 and/or the parameters used for that expression in Figure 12. We already noted in ref 24 that very large bowing parameters, such as b^{SiSn}, tend to be compositional dependent, and this could be the reason for the discrepancy. Concurrently, the neglect of third- or fourth-order terms in the polynomial expansion may not be entirely justified. The elucidation of this problem will require additional measurements over a broad compositional range as well as a detailed study of the binary alloy $Si_{1-y}Sn_y$. Very thin (<30 nm) films of $Si_{1-y}Sn_y$ have been demonstrated on GeSn-buffered Si using Si_3H_8 and SnD_4 precursors.[26] The introduction of higher-order silanes may represent an opportunity to grow thicker films suitable for detailed studies of their optical properties.

Because of the practical importance of GeSiSn alloys with the range of compositions used in this Article, in ref 14 we have also fit the measured E_0 values with a purely empirical expression that is bilinear in the Si and Sn compositions. Following the same procedure with our extended set of samples, we now obtained (in eV):

$$E_0(x, y) = 0.803 + (1.86 \pm 0.34)x - (2.40 \pm 1.4)y \tag{7}$$

We notice that the linear terms in eq 6 are $E_0^{Si} - E_0^{Ge} - b^{GeSi} = 3.08$ eV and $E_0^{Sn} - E_0^{Ge} - b^{GeSn} = -3.42$ eV. The much lower experimental x-coefficient (1.86 eV vs 3.08 eV) is thus the main reason why eq 6 systematically overestimates the E_0 energies. The predictions from eq 7 for our samples are also plotted as empty circles (red ○) in Figure 12, and we see that their agreement with experiment is excellent. However, given the entirely empirical nature of the bilinear expression (eq 7), it is not possible to assess its validity outside the Sn and Si compositional ranges explored in this work. For completeness, we also show in Figure 12, as a solid line, the prediction from eq 7 for GeSiSn alloys exactly lattice-matched to Ge.

III. CONCLUSION

In summary, a series of $Ge_{1-x-y}Si_xSn_y$ photodiodes was grown on conventional Ge wafers using a specially developed CVD approach based on ultralow temperature depositions of highly reactive Ge_4H_{10}, Si_4H_{10}, and SnD_4 hydrides. Ab initio thermochemistry calculations using Gaussian 03 indicate that an equimolar mixture of Si_4H_{10} and Ge_4H_{10} contains about twice as much of the reactive i-Ge_4H_{10} isomer in proportion to its i-Si_4H_{10} counterpart, in qualitative agreement with the experimental observation that an excess in Si_4H_{10} is needed to incorporate target amounts of silicon. Devices with compositions ranging from 5% to 20% Si and 1−5% Sn were fabricated and found to exhibit a clear and systematic shift in responsivity to higher IR energies relative to Ge, from 0.88 to 1.03 eV, while preserving the benefit of nearly strain-free lattice matching to bulk Ge. The latter has afforded superior microstructure in the as-grown devices, leading to the generation of low dark currents with a significant diffusion component, and enhanced responsivities relative to previous Sn-based group IV devices grown on Si. The results are particularly encouraging for photovoltaic applications of the ternary $Ge_{1-x-y}Si_xSn_y$ alloy, especially in the case of high efficiency multijunction designs requiring ~1 eV gap materials lattice-matched to the Ge platform. Finally, the development of analogous $Ge_{1-x-y}Si_xSn_y$ devices integrated on low cost Si wafers is envisioned by using intermediate Ge buffers to mitigate the impact of mismatch defects on diode performance.

■ AUTHOR INFORMATION

Corresponding Author

jkouvetakis@asu.edu

Notes

The authors declare no competing financial interest.

■ ACKNOWLEDGMENTS

This work was supported by the U.S. Air Force under contract AFOSR FA9550-12-1-0208 (Dr. Gernot Pomrenke), and by the U.S. Department of Energy under contract DE-FG36-08GO18003. We thank Emcore Corp. for providing the Ge wafers.

■ REFERENCES

(1) Bauer, M.; Taraci, J.; Tolle, J.; Chizmeshya, A. V. G.; Zollner, S.; Smith, D. J.; Menendez, J.; Hu, C.; Kouvetakis, J. *Appl. Phys. Lett.* **2002**, *81*, 2992.

(2) Vincent, B.; Gencarelli, G.; Bender, H.; Merckling, C.; Douhard, B.; Petersen, D. H.; Hansen, O.; Henrichsen, H. H.; Meersschaut, J.; Vandervorst, W.; Heyns, M.; Loo, R.; Caymax, M. *Appl. Phys. Lett.* **2011**, *99*, 152103.

(3) Gencarelli, F.; Vincent, B.; Souriau, L.; Richard, O.; Vandervorst, W.; Loo, R.; Caymax, M.; Heyns, M. *Thin Solid Films* **2012**, *520*, 3211.

(4) Sun, G.; Cheng, H. H.; Menendez, J.; Khurgin, J. B.; Soref, R. A. *Appl. Phys. Lett.* **2007**, *90*, 251105.

(5) Menendez, J.; Kouvetakis, J. *Appl. Phys. Lett.* **2004**, *85*, 1175.

(6) D'Costa, V. R.; Fang, Y. Y.; Tolle, J.; Kouvetakis, J.; Menéndez, J. *Thin Solid Films* **2010**, *518*, 2531.

(7) Beeler, R. T.; Smith, D. J.; Kouvetakis, J.; Menendez, J. *IEEE J. Photovolt.* **2012**, *3*, 434−440.

(8) Chroneos, A.; Jiang, C.; Grimes, R. W.; Schwingenschlögl, U.; Bracht, H. *Appl. Phys. Lett.* **2009**, *95*, 112101.

(9) Fang, Y.-Y.; Xie, J.; Tolle, J.; Roucka, R.; D'Costa, V. R.; Chizmeshya, A. V. G.; Menendez, J.; Kouvetakis, J. *J. Am. Chem. Soc.* **2008**, *130*, 16095.

(10) Bauer, M.; Ritter, C.; Crozier, P. A.; Ren, J.; Menéndez, J.; Wolf, G.; Kouvetakis, J. *Appl. Phys. Lett.* **2003**, *83*, 2163.

(11) Xie, J.; Tolle, J.; D'Costa, V. R.; Chizmeshya, A. V. G.; Menéndez, J.; Kouvetakis, J. *Appl. Phys. Lett.* **2009**, *95*, 181909.

(12) Xie, J.; Chizmeshya, A. V. G.; Tolle, J.; D'Costa, V. R.; Menendez, J.; Kouvetakis, J. *Chem. Mater.* **2010**, *22*, 3779.

(13) D'Costa, V. R.; Fang, Y.; Mathews, J.; Roucka, R.; Tolle, J.; Menendez, J.; Kouvetakis, J. *Semicond. Sci. Technol.* **2009**, *24*, 115006.

(14) Beeler, R. T.; Xu, C.; Smith, D. J.; Grzybowski, G.; Menéndez, J.; Kouvetakis, J. *Appl. Phys. Lett.* **2012**, *101*, 221111.

(15) Doolittle, L. R. *Nucl. Instrum. Methods Phys. Res., Sect. B* **1985**, *9*, 344.

(16) Grzybowski, G.; Beeler, R.; Chizmeshya, A. V. G.; Watkins, T.; Jiang, L.; Kouvetakis, J.; Menendez, J. *Chem. Mater.* **2012**, *24*, 1619−1628.

(17) Chung, K. H.; Yao, N.; Benziger, J.; Sturm, J. C.; Singh, K. K.; Carlson, D.; Kuppurao, S. *Appl. Phys. Lett.* **2008**, *92*, 113506.

(18) Frisch, M. J.; Trucks, G. W.; Schlegel, H. B.; Scuseria, G. E.; Robb, M. A.; Cheeseman, J. R.; Montgomery, J. A., Jr.; Vreven, T.; Kudin, K. N.; Burant, J. C.; Millam, J. M.; Iyengar, S. S.; Tomasi, J.; Barone, V.; Mennucci, B.; Cossi, M.; Scalmani, G.; Rega, N.; Petersson, G. A.; Nakatsuji, H.; Hada, M.; Ehara, M.; Toyota, K.; Fukuda, R.; Hasegawa, J.; Ishida, M.; Nakajima, T.; Honda, Y.; Kitao, O.; Nakai, H.; Klene, M.; Li, X.; Knox, J. E.; Hratchian, H. P.; Cross, J. B.; Bakken, V.; Adamo, C.; Jaramillo, J.; Gomperts, R.; Stratmann, R. E.; Yazyev, O.; Austin, A. J.; Cammi, R.; Pomelli, C.; Ochterski, J. W.; Ayala, P. Y.; Morokuma, K.; Voth, G. A.; Salvador, P.; Dannenberg, J. J.; Zakrzewski, V. G.; Dapprich, S.; Daniels, A. D.; Strain, M. C.; Farkas, O.; Malick, D. K.; Rabuck, A. D.; Raghavachari, K.; Foresman, J. B.; Ortiz, J. V.; Cui, Q.; Baboul, A. G.; Clifford, S.; Cioslowski, J.; Stefanov, B. B.; Liu, G.; Liashenko, A.; Piskorz, P.; Komaromi, I.; Martin, R. L.; Fox, D. J.; Keith, T.; Al-Laham, M. A.; Peng, C. Y.; Nanayakkara, A.; Challacombe, M.; Gill, P. M. W.; Johnson, B.; Chen, W.; Wong, M. W.; Gonzalez, C.; Pople, J. A. *Gaussian 03*, revision C.02; Gaussian, Inc.: Wallingford, CT, 2004.

(19) Weng, C.; Kouvetakis, J.; Chizmeshya, A. V. G. *J. Comput. Chem.* **2011**, *32*, 835−853.

(20) Ortiz, J. V.; Mintmire, J. W. *J. Am. Chem. Soc.* **1988**, *110*, 4522.

(21) Ritter, C. J.; Hu, C.-W.; Chizmeshya, A. V. G.; Tolle, J.; Nieman, R.; Tsong, I. S. T.; Kouvetakis, J. *J. Am. Chem. Soc.* **2006**, *128*, 6919.

(22) Roucka, R.; Mathews, J.; Weng, C.; Beeler, R.; Tolle, J.; Menendez, J.; Kouvetakis, J. *IEEE J. Quantum Electron.* **2011**, *47*, 213.

(23) Roucka, R.; Beeler, R.; Mathews, J.; Ryu, M.-Y.; Yeo, Y. K.; Menéndez, J.; Kouvetakis, J. *J. Appl. Phys.* **2011**, *109*, 103115.

(24) D'Costa, V. R.; Fang, Y. Y.; Tolle, J.; Kouvetakis, J.; Menendez, J. *Phys. Rev. Lett.* **2009**, *102*, 107403.

(25) D'Costa, V. R.; Cook, C. S.; Birdwell, A. G.; Littler, C. L.; Canonico, M.; Zollner, S.; Kouvetakis, J.; Menendez, J. *Phys. Rev. B* **2006**, *73*, 125207.

(26) Tolle, J.; Chizmeshya, A. V. G.; Fang, Y. Y.; Kouvetakis, J.; D'Costa, V. R.; Hu, C. W.; Menéndez, J.; Tsong, I. S. T. *Appl. Phys. Lett.* **2006**, *89*, 231924.